Monthly Notices
of the
ROYAL ASTRONOMICAL SOCIETY

MNRAS **474,** 1705–1717 (2018)
Advance Access publication 2017 November 6

doi:10.1093/mnras/stx2865

# Hubble PanCET: an isothermal day-side atmosphere for the bloated gas-giant HAT-P-32Ab

N. Nikolov,[1★] D. K. Sing,[1] J. Goyal,[1] G. W. Henry,[2] H. R. Wakeford,[1] T. M. Evans,[1] M. López-Morales,[3] A. García Muñoz,[4] L. Ben-Jaffel,[5] J. Sanz-Forcada,[6] G. E. Ballester,[7] T. Kataria,[8] J. K. Barstow,[9] V. Bourrier,[10] L. A. Buchhave,[11] O. Cohen,[12] D. Deming,[13] D. Ehrenreich,[10] H. Knutson,[14] P Lavvas,[15] A. Lecavelier des Etangs,[5] N. K. Lewis,[16] A. M. Mandell[17] and M. H. Williamson[2]

*Affiliations are listed at the end of the paper*

Accepted 2017 October 31. Received 2017 October 11; in original form 2017 August 5

## ABSTRACT

We present a thermal emission spectrum of the bloated hot Jupiter HAT-P-32Ab from a single eclipse observation made in spatial scan mode with the Wide Field Camera 3 (WFC3) aboard the Hubble Space Telescope (*HST*). The spectrum covers the wavelength regime from 1.123 to 1.644 μm which is binned into 14 eclipse depths measured to an averaged precision of 104 parts-per million. The spectrum is unaffected by a dilution from the close M-dwarf companion HAT-P-32B, which was fully resolved. We complemented our spectrum with literature results and performed a comparative forward and retrieval analysis with the 1D radiative-convective ATMO model. Assuming solar abundance of the planet atmosphere, we find that the measured spectrum can best be explained by the spectrum of a blackbody isothermal atmosphere with $T_{\rm p} = 1995 \pm 17$ K, but can equally well be described by a spectrum with modest thermal inversion. The retrieved spectrum suggests emission from VO at the WFC3 wavelengths and no evidence of the 1.4 μm water feature. The emission models with temperature profiles decreasing with height are rejected at a high confidence. An isothermal or inverted spectrum can imply a clear atmosphere with an absorber, a dusty cloud deck or a combination of both. We find that the planet can have continuum of values for the albedo and recirculation, ranging from high albedo and poor recirculation to low albedo and efficient recirculation. Optical spectroscopy of the planet's day-side or thermal emission phase curves can potentially resolve the current albedo with recirculation degeneracy.

**Key words:** techniques: spectroscopic – planets and satellites: atmospheres – planets and satellites: individual: HAT-P-32Ab – stars: individual: HAT-P-32A.

## 1 INTRODUCTION

Transit, secondary eclipse (occultation) and phase curve observations provide an unprecedented access to the chemical composition, scattering and absorption from clouds and hazes, vertical thermal structure and recirculation of planetary atmospheres beyond the Solar system (Seager 2010; Winn 2010; Pont et al. 2013; Heng 2017). A comparative transmission study of 10 hot-Jupiter exoplanets showed that similar to Solar system planets, where clouds and hazes are present on every planet with an atmosphere, exoplanets also have clouds and hazes in a continuum with a lack of temperature dependance (Sing et al. 2016). Complementary to transit spectroscopy, which is sensitive to absorbing and scattering constituents (e.g. atomic sodium and potassium, water vapour, clouds and hazes) located in the upper atmosphere at the day–night terminator (Sing et al. 2011, 2016; Nikolov et al. 2014, 2015, 2016; Evans et al. 2016; Gibson et al. 2017), observations of an exoplanetary occultation, i.e. when the planet passes behind its host star, probe the deeper and hotter layers of the day-side hemisphere. Most of the secondary eclipse observations are made for short-period hot-Jupiter exoplanets (i.e. with high temperature and large radii to produce deep eclipses) and at near- and mid-infrared wavelengths (mainly with the *Hubble* and *Spitzer Space Telescopes*), where the planets are bright and the host stars are correspondingly faint (Madhusudhan et al. 2014). Sensitive to the deeper layers of the atmosphere secondary eclipse observations can constrain the vertical temperature structure, chemistry and heat recirculation of exoplanets

★ E-mail: nikolov.nkn@gmail.com

(Burrows et al. 2007; Knutson et al. 2008; Fortney et al. 2010). High-precision observations can distinguish an isothermal (blackbody), decreasing with height (non-inverted) or increasing with height (inverted) thermal profiles. In the first case, the emission spectrum of the planetary atmosphere would be featureless with a lack of absorbing or emitting features (e.g. $H_2O$, CO, $CH_4$, depending on the wavelength). An isothermal or blackbody spectrum indicates that either the temperature remains constant at each layer or alternatively that the same pressure level (altitude) is probed by the spectrum, i.e. the radiation originates from a cloud deck and the measured brightness temperature is the temperature of the cloud near the altitude where the cloud becomes optically thick, i.e. at $\tau \sim 1$. If the planetary atmosphere contains layers where temperature decreases uniformly with altitude, the resulting thermal spectrum is expected to exhibit absorption features (Stevenson et al. 2014a). On the contrary, if a hotter layer is located above a cooler region (stratosphere) the first will produce a thermal spectrum with the same features observed in emission (Madhusudhan et al. 2014; Evans et al. 2017). Theoretical studies have predicted that the spectroscopically active gasses TiO and VO could capture the incident stellar radiation and consequently have been proposed as the responsible constituent for thermally inverted stratospheres (Hubeny, Burrows & Sudarsky 2003; Fortney et al. 2008). Previous studies have demonstrated that the population of hot Jupiters are a rather heterogenous group with some of them showing spectra consistent with thermal inversion layer caused by TiO (Haynes et al. 2015) or an unknown absorber and others have spectra consistent with no inversion layers (Fortney et al. 2008; Line et al. 2014, 2016; Zhao et al. 2014). Using *HST* WFC3 Evans et al. (2017) recently reported compelling evidence of detection of a stratosphere in the very hot ($T_p = 2700 \pm 10$ K) Jupiter WASP-121b, where the 1.4 μm water feature has been resolved and observed in emission.

In this paper, we report measurements from a single *HST* WFC3 secondary eclipse observation of HAT-P-32Ab. Our measured thermal emission spectrum is consistent with radiation from an isothermal blackbody, but can equally well be described by a model with thermal inversion. This result is part of the *HST* Panchromatic Comparative Exoplanet Treasury (PanCET) program, which targets 20 exoplanets for the first large-scale simultaneous UltraViolet, Optical, Infrared (UVOIR) comparative study of exoplanets (Evans et al. 2017; Wakeford et al. 2017). A major aim of PanCET is to produce one of the first comparative studies of clouds and hazes in exoplanet atmospheres over a wide range of parameters such as temperature, metallicity, mass and radius. This paper is organized as follows: in Section 2 we report the observations, reductions and light-curve analysis, the thermal spectrum is reported and discussed in Section 3 and Section 4 presents our conclusions.

## 2 OBSERVATIONS AND ANALYSIS

### 2.1 The hot Jupiter HAT-P-32Ab

The target of our study HAT-P-32Ab, is a standout highly inflated hot Jupiter ($M_p = 0.860 \pm 0.164\,M_{Jup}$, $R_p = 1.789 \pm 0.025\,R_{Jup}$ and an equilibrium temperature $T_{eq} = 1786 \pm 26$ K) on a circular orbit with period of $P = 2.15$ d around a moderately bright ($J = 10.251 \pm 0.022$) late-F-type dwarf star in the northern constellation Andromeda (Hartman et al. 2011; Zhao et al. 2014). Observations of the Rossiter–McLaughlin effect showed that the rotation axis of the star nearly lays in the plane of the planetary orbit $85^\circ \pm 2^\circ$ implying a highly misaligned system (Albrecht et al. 2012). Using adaptive optics Adams et al. (2013) detected a candidate M-dwarf companion (HAT-P-32B), which was confirmed (at a separation of $2\farcs923 \pm 0\farcs004$ and position angle $110\fdg64 \pm 0^\circ$; Zhao et al. 2014) and shown to be physically associated with HAT-P-32A (Knutson et al. 2014). Combining broad-band ground-based *Hale* WIRC and *Spitzer* IRAC 3.6 and 4.5 μm photometric observations of the secondary eclipse of HAT-P-32Ab, Zhao et al. (2014) concluded that the thermal emission spectrum of the planet is equally well described by a model assuming thermal inversion and a blackbody model with planet temperature $T_p = 2042 \pm 50$ K. With one of the strongest transmission signals compared to similar hot Jupiters ($\Delta\delta \approx 2(H/R_p)(R_p/R_*)^2 \sim 350$ ppm for 1 pressure scaleheight, $H$; Winn 2010), HAT-P-32Ab has been extensively followed up with optical transmission spectroscopy. While theory of irradiated gas giants (e.g. Fortney et al. 2010) predicted broad sodium, potassium and TiO/VO absorption features for clear atmospheres at visible wavelengths, a number of optical studies reported a featureless flat transmission spectrum, suggesting a thick cloud deck at the day–night terminator of the planet Gibson et al. (2013a), Mallonn et al. (2016), Mallonn & Strassmeier (2016) and Nortmann et al. (2016).

### 2.2 *HST* WFC3 observations

We observed a single secondary eclipse of HAT-P-32Ab with *HST* WFC3 on UT 2016 December 18 as part of Program 14767 (PIs Sing and López-Morales). Time series of spectra were collected with grism G141, which covers the wavelength range from 1.1 to 1.7 μm at a resolution of $R = \lambda/\Delta\lambda = 130$ and a dispersion of 4.7 nm pixel$^{-1}$. The target was monitored for 7.4 h during five consecutive orbits, covering the full eclipse, which lasted for 3.1 h. The first, second and fifth *HST* orbits cover out of eclipse phases and the third and fourth orbits are in the eclipse. Target acquisition was performed in imaging mode with an exposure time of 4.94 s with the F139M filter. An inspection of the acquisition image showed the physically associated HAT-P-32B M-dwarf companion to be spatially resolved from the target. During each of the following spectroscopic observations, the telescope pointing was scanned along the cross-dispersion axis of the detector. This spreads the stellar flux across more pixels compared to a fixed pointing observation, allowing for a longer exposure times with higher duty cycle. We used forward scanning with a rate of 0.05 arcsec s$^{-1}$. To reduce overheads we used a 256 × 256 subarray containing the target spectrum. We used the SPARS10 sampling sequence with fourteen non-destructive reads per exposure (NSAMP = 14) resulting in total integration times of 88.44 s and scans across 38 pixel rows of the cross-dispersion axis. Typical count levels reached a maximum of $3.1 \times 10^4$ analogue-to-digital units (ADU), i.e. well within the linear regime of the detector. A total of 88 spectra were collected over the five *HST* orbits with 16 of them covering the first and 18 exposures obtained during each of the remaining four orbits.

### 2.3 Reductions and calibrations

We started the analysis with the `ima` 2D spectra produced by the CalWFC3 pipeline (v3.1.6), which already had basic calibrations including dark subtraction and flat-field correction. We extracted flux for HAT-P-32A from each exposure by taking the difference between successive non-destructive reads. For each read difference, we removed the background by taking the median flux in a box of pixels well away from the stellar spectra. Typical background levels integrated over the 88.44 s exposures started between ∼130

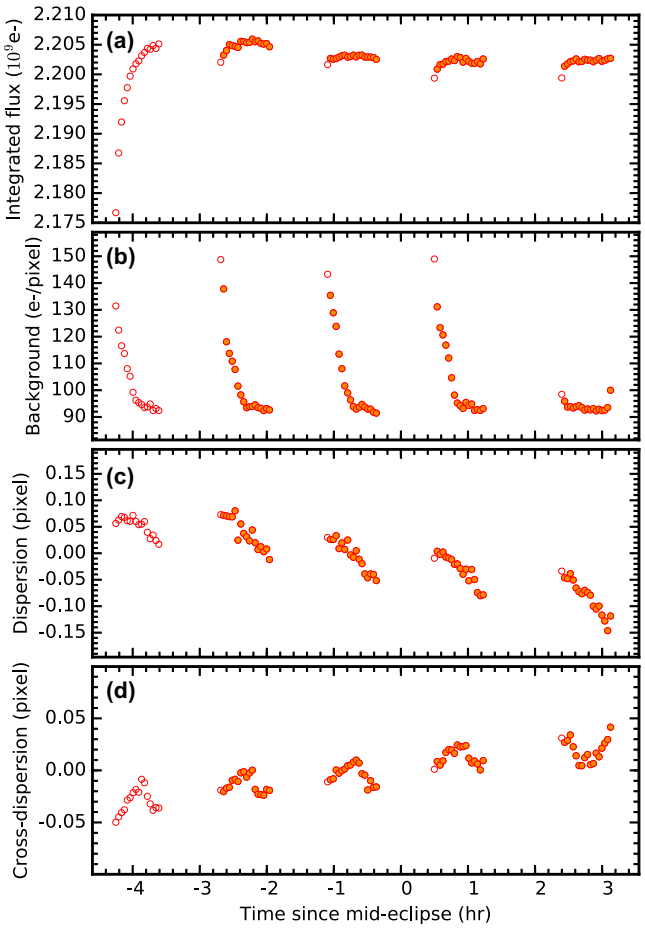


**Figure 1.** White light curve and auxiliary variable time series for HAT-P-32A. Open symbols indicate data that has been discarded and filled circles indicate the data that were retained for light-curve analysis. (a) Raw flux band-integrated light curve in units of electrons. We discarded the first full *HST* orbit, because it exhibits particularly steep ramp as well as the first exposure of each subsequent orbit. (b) Measured background for each frame in units of electrons, using the last individual read of each full scan. (c) Median-subtracted drift of the spectra along the dispersion axis in units of pixels, estimated by cross-correlating the spectra with a reference spectrum. (d) Same as the previous panel, but for the cross-dispersion axis measured with flux-weighted mean.

and 150 electrons per pixel and decreased to ∼90 electrons per pixel over each HST orbit (see Fig. 1). We then determined the flux-weighted centre of the HAT-P-32A scan and set to zero all pixel values located more than 14 pixels above and below along the cross-dispersion axis. Application of this top hat filter had the effect of masking the flux contributions from nearby contaminating stars including the companion HAT-P-32B located at ∼23 px from the centre of the target. It had the additional advantage of eliminating many of the pixels affected by cosmic rays. The final reconstructed images were produced by adding together the read differences for each exposure.

Any remaining cosmic rays were identified by scanning each individual spectrum along the dispersion axis. For each scan, we examined its difference with a median combined point-spread function (PSF) profile, computed using the five preceding and five following consecutive columns. Before taking the difference we scaled the median profile to the scanned column. Pixels deviating $>4\sigma$ were flagged as transient outliers and subsequently replaced by their corresponding value from a nominal PSF profile, i.e. identical to the median combined PSF profile, but scaled to the column values, ignoring each of the flagged pixels as in Nikolov et al. (2014). Compared to other algorithms, e.g. temporal filtering, this cosmic ray identification approach has the advantage to be independent of spatial scan inhomogeneities, e.g. read-out delays, which lead to extra flux accumulated typically in a few images of the time series. We flagged between 0 and ∼15 pixels per reconstructed image. Our light-curve analysis (see below) was largely unaffected by whether or not we identified and corrected for cosmic ray events, although for two of the images it reduced the scatter of the best-fitting light-curve residual.

We extracted target spectra using a fixed-size box by summing the flux of all pixels. The box had dimensions of 176 × 52 pixels, and centred for each individual exposure. To identify the box position along the dispersion and cross-dispersion axis we took the flux-weighted mean of each 2D spectrum. We found the target drifted on the dispersion and cross-dispersion axis by 0.3 and 0.1 pixels, respectively (see Fig. 1).

The wavelength solution was established by cross-correlating each target spectrum against a Kurucz stellar spectrum model (Kurucz 1979) with properties similar to the HAT-P-32 host star: $T_{\rm eff} = 6207 \pm 88$ K, $\log g = 4.33 \pm 0.01$ and [Fe/H] $= -0.04 \pm 0.08$ (Hartman et al. 2011).

### 2.4 White light-curve analysis

We computed the WFC3/G141 band-integrated 'white' light curve by summing the flux of each stellar spectrum along the dispersion axis and across the wavelength range from 1.123 to 1.644 μm (Fig. 2). This wavelength range was chosen for the white and spectroscopic light curves to avoid the steep edges of the G141 grism response. The white light curve exhibits quasi-repeatable systematics which are considered to originate from charge trapping in the detector (Deming et al. 2013; Huitson et al. 2013; Zhou et al. 2017). We modelled the secondary eclipse and instrumental systematics simultaneously by treating the data as a Gaussian process (GP) similar to the methodology of Gibson et al. (2013a,b, 2017) and Evans et al. (2016, 2017). The GP analysis in this study has been performed with the Python GP library `george` (Ambikasaran et al. 2014; Foreman-Mackey 2015; Foreman-Mackey 2016). Under the GP assumption, the data likelihood is a multivariate normal distribution with a mean function $\boldsymbol{\mu}$ describing the deterministic eclipse signal and a covariance matrix $\boldsymbol{K}$ that accounts for stochastic correlations (i.e. poorly constrained systematics) in the data:

$$p(\boldsymbol{f}|\boldsymbol{\theta}, \boldsymbol{\gamma}) = \mathcal{N}(\boldsymbol{\mu}, \boldsymbol{K}), \quad (1)$$

where $p$ is the probability density function, $\boldsymbol{f}$ is a vector containing the flux measurements, $\boldsymbol{\theta}$ is a vector containing the mean function parameters, $\boldsymbol{\gamma}$ is a function containing the covariance parameters and $\mathcal{N}$ is a multivariate normal distribution. We defined the mean function $\boldsymbol{\mu}$ as follows:

$$\boldsymbol{\mu}(t,\ \hat{\boldsymbol{t}};\ c_0,\ c_1,\ \delta,\ T_{\rm mid}) = [c_0 + c_1\hat{\boldsymbol{t}}]\ E(t; F_{\rm p}/F_*, T_{\rm mid}), \quad (2)$$

where $t$ is a vector of all central exposure time stamps in Julian Date (JD), $\hat{\boldsymbol{t}}$ is a vector containing all standardized times, i.e. with subtracted mean exposure time and dived by the standard deviation, $c_0$ and $c_1$ describe a linear baseline trend, $E$ is an analytical expression describing the secondary eclipse, $F_{\rm p}/F_*$ is the planet-to-star flux ratio, $\delta = (F_{\rm p}/F_*)(R_{\rm p}/R_*)^2$ is the eclipse depth and $T_{\rm mid}$ is the eclipse central time. To obtain an analytical eclipse model $E$, we used a Mandel & Agol (2002) transit model with limb darkening

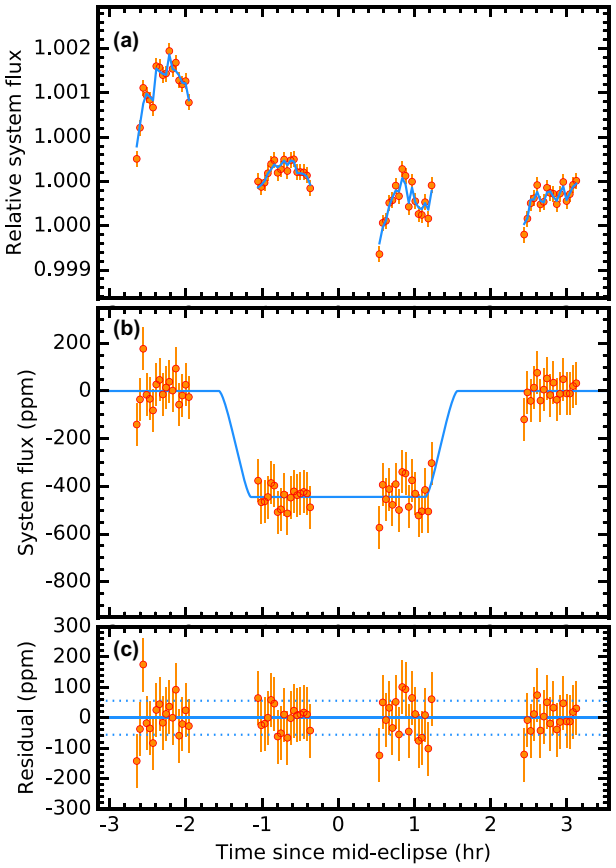


**Figure 2.** White light curve for HAT-P-32Ab. (a) Raw flux, normalized to the median out-of transit baseline along with the photon noise uncertainties. The blue continuous lines indicate the best-fitting GP model. The gaps in the data are a result of the target being occulted by the Earth during each *HST* orbit. (b) Normalized system flux and the best-fitting eclipse light curve after the best-fitting GP systematics model has been removed. (c) Data minus best-fitting model residuals with the fitted (rescaled photon noise) error-bars. The dotted lines indicate the residual dispersion.

**Table 1.** System parameters.

| Parameter | Value |
|---|---|
| $P$ (d) | 2.150 009, fixed |
| $e$ | 0, fixed |
| $\omega$ (°) | 0, fixed |
| $i$ (°) | 88.90, fixed |
| $a/R_*$ | 6.05, fixed |
| $R_p/R_*$ | 0.1508, fixed |
| $T_{mid}$ (JD) | $2\,457\,741.119\,4^{+0.0031}_{-0.0029}$ |
| $(F_p/F_*)(R_p/R_*)^2$ (ppm) | $445^{+72}_{-73}$ |
| $c_0$ | $1.000\,3^{+0.000\,15}_{-0.000\,19}$ |
| $c_1$ | $(-4.5 \pm 6.9) \times 10^{-5}$ |
| A (ppm) | $368^{+162}_{-93}$ |
| $\ln \tau_\phi$ | $-0.32^{+1.04}_{-0.95}$ |
| $\ln \tau_x$ | $-0.3^{+1.1}_{-0.9}$ |
| $\ln \tau_y$ | $2.5^{+1.7}_{-1.5}$ |
| $\sigma_w$ (ppm) | $57^{+39}_{-37}$ |

set to zero. We fixed the remaining system parameters to literature values listed in Table 1 and fitted only for the eclipse depth and central time. The covariance matrix is defined as

$$\boldsymbol{K} = \sigma_i^2 \delta_{ij} + k_{ij}, \tag{3}$$

where $\sigma_i$ are the photon noise uncertainties, $\delta_{ij}$ is the Kronecker delta function and $k_{ij}$ is a covariance function or kernel. In our light-curve fitting, we assumed the white noise term was the same for all data points and allowed it to vary as a free parameter, $\sigma_w$. In this study, we choose to use the Matérn $\nu = 3/2$ kernel with *HST* orbital phase $\phi$, dispersion drift $x$ and cross-dispersion drift $y$ as input variables. As with the linear time term, we also standardized the three input parameters ($\phi$, $x$ and $y$) prior to fitting the light curve. The covariance function then was defined as:

$$k_{ij} = A^2 \left(1 + \sqrt{3} D_{ij}\right) \exp\left(-\sqrt{3} D_{ij}\right), \tag{4}$$

where $A$ is the characteristic correlation amplitude and

$$D_{ij} = \sqrt{\frac{(\hat{\phi}_i - \hat{\phi}_j)^2}{\tau_\phi^2} + \frac{(\hat{x}_i - \hat{x}_j)^2}{\tau_x^2} + \frac{(\hat{y}_i - \hat{y}_j)^2}{\tau_y^2}}, \tag{5}$$

where $\tau_\phi$, $\tau_x$ and $\tau_y$ are the correlation length scales and the hatted variables are standardized. In the white light-curve fitting, we allowed parameters $\boldsymbol{\theta} = [c_0, c_1, F_p/F_*, T_{mid}]$ and $\boldsymbol{\gamma} = [A, \tau_\phi, \tau_x, \tau_y]$ to vary and fixed the planet-to-star radius ratio $R_p/R_*$, orbital inclination $i$ and orbital period $P$ to their literature values (Hartman et al. 2011). Our prior distribution had the form $p(\boldsymbol{\theta}, \boldsymbol{\gamma}) = p(c_0)\, p(c_1)\, p(F_p/F_*)\, p(T_{mid})\, p(A) p(\tau_\phi)\, p(\tau_x)\, p(\tau_y)$. Uniform priors were adopted for $p(c_0)$, $p(c_1)$, $p(F_p/F_*)$, $p(T_{mid})$. Log-uniform priors were adopted for $p(A)$, $p(\tau_\phi)$, $p(\tau_x)$, $p(\tau_y)$.

Prior to fitting all light-curves, we discarded the data from the first full *HST* orbit, because of the particularly strong ramp systematic it exhibited. In addition, we also discarded the first data point of each of the subsequent four orbits as they had significantly lower flux compared to the rest of the data in the same orbit.

We used the Markov-Chain Monte Carlo (MCMC) Python software package EMCEE (Foreman-Mackey et al. 2013) to marginalise the posterior distribution $p(\boldsymbol{\theta}, \boldsymbol{\gamma} | \boldsymbol{f}) \propto p(\boldsymbol{f} | \boldsymbol{\theta}, \boldsymbol{\gamma})\, p(\boldsymbol{\theta}, \boldsymbol{\gamma})$. We initialized three groups of 150 walkers close to the maximum likelihood solution, which was located using the Levenberg–Marquardt least-squares algorithm as implemented in the MPFIT.[1] Groups one and two were run for 350 samples and the third group had 2500 samples. Before running for the second group we re-sampled the positions of the walkers in a narrow space around the position of the best walker from the first run. This extra re-sampling step was useful because otherwise some of the walkers can start in a low likelihood area of parameter space and would require more computational time to converge. An eclipse model computed using the marginalized posterior distributions for the depth and central time is shown in Fig. 2 and the parameter values are reported in Table 1. We find the eclipse central time to be constrained to only ∼4.3 min. Such high uncertainty is explained with the insufficient phase coverage during the ingress and egress portions of the eclipse light curve. The residuals using the best-fitting model from this analysis were found to be within 2 per cent of the theoretical the photon noise expectation. The posterior distributions for all fitting parameters of the white light curve are shown in Appendix A.

### 2.5 Spectroscopic light-curve analysis

We produced 14 spectroscopic light curves across the wavelength range from 1.123 to 1.644 μm by summing the flux of the stellar spectra in bins with widths of 8 pixels each (equivalent to 0.037 μm).

[1] http://www.physics.wisc.edu/craigm/idl/fitting.html

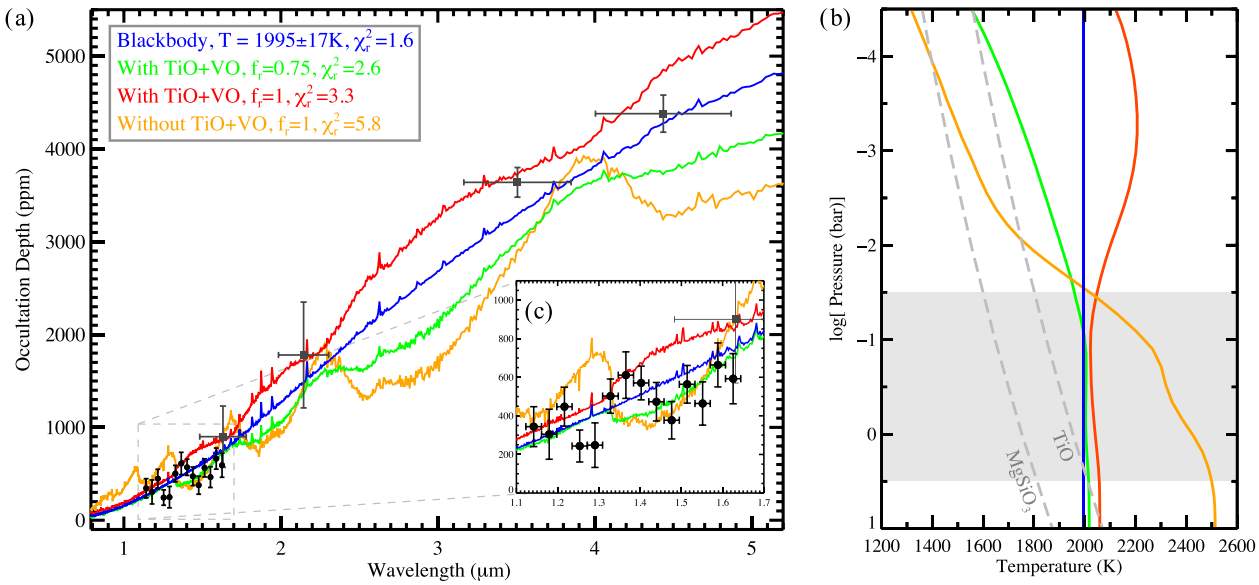


**Figure 3.** Emission spectrum of HAT-P-32Ab, forward models and assumed pressure–temperature profiles. (a) Combined WFC3 emission spectrum of HAT-P-32Ab (black dots) with the dilution-corrected *Hale* WIRC $H$ and $K_S$ and *Spitzer* IRAC 3.6 and 4.5 μm eclipse observations (grey dots) detailed in Zhao et al. 2014. The continuous lines indicate atmospheric models fit to the spectrum. The top two best-match models assume an isothermal and thermally inverted pressure–temperature profiles. Models assuming decreasing temperature with an increasing altitude are excluded at high confidence. (b) Zoom around the the WFC3 spectrum with models. (c) Pressure–temperature profiles assumed in the calculation of the emission models. The shaded region indicates the pressures probed by our WFC3 observations and the dashed lines indicate condensation curves for atmospheric constituents $CaSiO_3$ and TiO.

We removed wavelength-independent systematics using a common-mode correction. This is a powerful technique used in a number of previous works from both space and the ground (Sing et al. 2012; Deming et al. 2013; Gibson et al. 2013a,b; Huitson et al. 2013; Nikolov et al. 2015, 2016). To compute the common-mode we divided the raw white light curve to an eclipse model. We computed the eclipse model using the central time $T_{\rm mid}$ and occultation depth from the marginalized posterior distributions of the white light-curve fit and the adopted orbital period, inclination and normalized semimajor axis from Table 1. Prior to fitting, we corrected the raw spectroscopic light curves by dividing each of them to the common-mode light curve (see Fig. B1). The common-mode technique relies on the similarities of time dependent systematics, which can be characterized by the light curves themselves and removed individually for each spectral wavelength bin. Empirically determining and removing systematics has an advantage over a parametrized method, as higher order frequencies are naturally subtracted.

We performed fits to the common-mode corrected spectroscopic light curves adopting the same data likelihood and uniform prior distributions as for the white light-curve analysis. However, we allowed only the eclipse depth to vary and fixed the central time to its white light value. The results from our analysis are reported in Table 2 and the eclipse models, calculated using the parameter values from the corresponding marginalized distributions, are shown in Fig. B1. For all of the 14 bands, we found a median scatter of 104 parts per million close to the photon noise. The measured wavelength-dependent secondary eclipse (occultation) depths, which comprise our thermal emission spectrum of HAT-P-32b are plotted in Fig. 3.

**Table 2.** Thermal eclipse spectrum of HAT-P-32b.

| Wavelength (μm) | Eclipse depth (ppm) |
|---|---|
| 1.123–1.161 | $344^{+100}_{-103}$ |
| 1.161–1.198 | $305^{+127}_{-125}$ |
| 1.198–1.235 | $448^{+95}_{-103}$ |
| 1.235–1.272 | $244^{+81}_{-83}$ |
| 1.272–1.309 | $248^{+110}_{-115}$ |
| 1.309–1.347 | $502^{+87}_{-87}$ |
| 1.347–1.384 | $611^{+118}_{-119}$ |
| 1.384–1.421 | $570^{+86}_{-87}$ |
| 1.421–1.458 | $473^{+101}_{-98}$ |
| 1.458–1.495 | $377^{+96}_{-94}$ |
| 1.495–1.533 | $564^{+95}_{-97}$ |
| 1.533–1.570 | $464^{+109}_{-113}$ |
| 1.570–1.607 | $664^{+113}_{-111}$ |
| 1.607–1.644 | $592^{+134}_{-126}$ |

### 2.6 Ground-based photometry of HAT-P-32A

Stellar activity can complicate the interpretation of transmission and emission spectra (with limited effect on infrared emission spectroscopy, Zellem et al. 2017) but can be corrected for if complimentary ground-based photometry is available (e.g. HD 189733; Sing et al. 2011). Therefore, we scheduled nightly photometry of HAT-P-32A on the Tennessee State University Celestron 14-inch (C14) automated imaging telescope (AIT) at Fairborn Observatory (see e.g. Henry 1999; Eaton, Henry & Fekel 2003). We have acquired a total of 223 nightly observations during the 2014–15, 2015–16 and 2016–17 observing seasons. The observations were made with a Cousins R filter and an SBIG STL-1001E CCD camera. Differential magnitudes were computed with respect to the mean brightness of 10 of the most constant comparison stars in the same field. Further details of our data acquisition, reduction procedures

**Table 3.** Summary of AIT photometric observations of HAT-P-32A.

| Observing season | $N_{obs}$ | Date range HJD−2400000 | Sigma (mag) | Seasonal mean (mag) |
|---|---|---|---|---|
| 2014-15 | 82 | 56943–57114 | 0.003 02 | −0.472 10 ± 0.000 33 |
| 2015-16 | 85 | 57293–57472 | 0.003 01 | −0.471 85 ± 0.000 33 |
| 2016-17 | 56 | 57705–57843 | 0.002 83 | −0.470 63 ± 0.000 38 |

and analysis of the data can be found in Sing et al. (2015), which describe a similar analysis of the planetary-host star WASP-31.

Our photometric observations are summarized in Table 3. Standard deviations of single nightly observations of HAT-P-32A with respect to their corresponding seasonal mean differential magnitudes are given in column 4; all are very close to 0.003 mag. This is the typical level of photometric precision achieved for a single observation with the AIT on good nights; see e.g. table 1 in both Kreidberg et al. (2015) and Sing et al. (2015). We performed periodogram analyses on each season and find no evidence for any periodicity between 1 and 100 d. In addition, the three seasonal means given in column 5 of Table 3 agree to within a standard deviation of only 0.000 079 mag. Therefore, we conclude that HAT-P-32A is constant, with the exception of transits, on both nightly and yearly time-scales to the limit of our photometric precision.

## 3 DISCUSSION

### 3.1 Thermal spectrum

We combined the WFC3 thermal emission spectrum with the dilution-corrected *Hale* WIRC $H$ and $K_S$ and *Spitzer* IRAC 3.6 and 4.5 μm eclipse observations detailed in Zhao et al. (2014). To further reduce a potential offset in the eclipse depths of the *Hale–Spitzer* photometry and the *HST* spectrum we adopted the system parameters of Zhao et al. (2014) when fitting the WFC3 light curves (see Table 1).

### 3.2 Blackbody and forward atmospheric models

We first fit a blackbody model to determine the temperature of the planet. For this, we used a BT-Settl stellar model atmosphere (Allard, Homeier & Freytag 2012) with the closest match to the effective temperature, surface gravity and metallicity of HAT-P-32A from Hartman et al. (2011). We found that the best-fitting model for the planet, with a $\chi^2 = 27$ for 17 degrees of freedom, and BIC = 30.1, corresponds to a $T_p = 1995 \pm 17$ K. This models correspond to the blue curve in Fig. 3. Our planet temperature measurement is consistent ($\sim 0.9\sigma$) with the temperature reported in Zhao et al. (2014), who found $T_p = 2042 \pm 50$ K.

We then performed forward modelling of the measured thermal emission spectrum using the 1D atmosphere ATMO code (Amundsen et al. 2014, 2017; Tremblin et al. 2015, 2016; Drummond et al. 2016; Goyal et al. 2017). ATMO computes the 1D pressure–temperature (P–T) atmospheric structure in plane-parallel geometry and also produces forward models assuming radiative, convective and chemical equilibrium. The code includes isotropic multi-gas Rayleigh scattering, $H_2$–$H_2$ and $H_2$–He collision-induced absorption as well as opacities for all major chemical species taken from the most up-to-date high-temperature sources, including: $H_2O$, $CO_2$, CO, $CH_4$, $NH_3$, Na, K, Li, Rb and Cs, TiO, VO, and FeH (Amundsen et al. 2014; Goyal et al. 2017). It uses the correlated-$k$ approximation with the random overlap method to compute the total gaseous mixture opacity, which has been shown to agree well with a full line-by-line treatment (Amundsen et al. 2014).

We computed P–T profiles using 50 vertical model levels with minimum and maximum optical depth of $10^{-5}$ and $2 \times 10^5$ at 1 μm, respectively. The P–T profiles were computed using 32 correlated-$k$ bands while spectra were computed using 5000 correlated-$k$ bands equally spaced in wavenumber between 1 and $5 \times 10^4$ cm$^{-1}$. Equilibrium chemistry calculations include condensation with rainout while computing P–T profiles.

We computed ATMO emission models, assuming P–T profiles of a decreasing (non-inverted), and an increasing (inverted) temperature with altitude. The models corresponding to each profile were computed assuming 0.25, 0.5, 0.75 and 1 for the recirculation factors ($f_r$), which govern the distribution of input stellar energy in the planet's atmosphere. A factor of unity implies no redistribution, while factor of a half implies efficient redistribution (Fortney & Marley 2007). In the calculation of the recirculation factor, we assumed an angle $\mu = 60°$.

To compare models with observations, we averaged the model spectra within the wavelength bins of the observed spectrum and computed the corresponding $\chi^2$. The results are shown in Fig. 3. From all the ATMO forward models, the data is best fit by a model with TiO/VO and a weak thermal inversion. However, that model, with reduced chi-square of $\chi^2_r = 2.6$ and BIC = 48.9, is a worse fit than the blackbody emission model described above ($\chi^2_r = 1.6$, BIC = 30.1). This analysis also reveals that ATMO models without thermal inversions (the orange and green lines in Fig. 3) are unlikely to explain the observed spectrum. Finally, the planets' emission spectrum shows no evidence of water, based on these fits.

### 3.3 Retrieval models

Besides computing forward models, ATMO can also be utilized as a retrieval tool to compute both emission and transmission spectra from an input P–T profile and arbitrary chemical abundances (see Section 3.3 and Evans et al. 2017; Wakeford et al. 2017). Several of the WFC3 measurements, which have the highest precision from all data points, deviate at the $\sim 2\sigma$ from the predicted absorption or emission water features. To further interpret the observed spectrum and constrain the planet P–T profile we turn to retrieval (Madhusudhan & Seager 2009; Line et al. 2013) analysis using ATMO.

Our retrieval approach follows the methodology detailed in Evans et al. (2017) and Wakeford et al. (2017). In summary, we fitted for the abundances of the molecules expected to add significant opacity in the wavelength region of our observations. In particular, we included $H_2O$, CO, $CO_2$, $CH_4$, $NH_3$, HCN, TiO and VO, assuming that those gasses are well-mixed vertically in the atmosphere. We assumed 50 pressure levels evenly spaced in log pressure between $10^{-8}$ and 500 bar in the model planetary atmosphere. For the P–T profile, we adopted the 1D analytic formulation of Guillot (2010), which assumes radiative equilibrium and is flexible enough to describe atmospheres with and without thermal inversion (stratosphere). When using the parametrized P–T profile, we fitted the data assuming either one or two visible channels. With this assumption we had 3–5 parameters for the P–T profile: the Planck mean thermal infrared opacity, $\kappa_{IR}$; the ratios of the optical to infrared opacities in the two channels, $\gamma_1$ and $\gamma_2$; a partition of the flux between the two optical channels, $\alpha$; and an irradiation efficiency factor, $\beta$. We assumed a value of $1.789 R_J$ for the planetary radius, corresponding to the lowest-altitude measured in transit observations at optical wavelengths. To model the input flux from the HAT-P-32A host

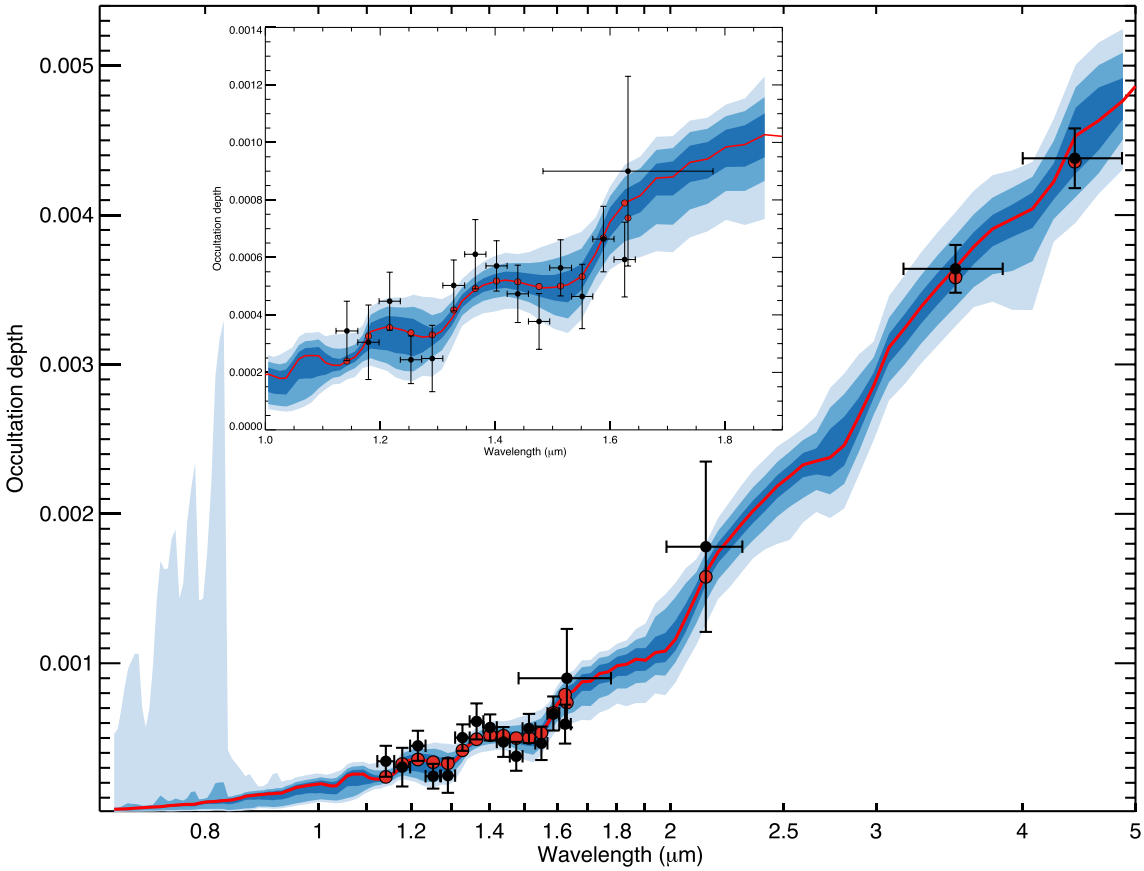


**Figure 4.** Emission spectrum of HAT-P-32Ab (dots with $1\sigma$ uncertainties) with model emission spectra (lines) binned to the resolution of the data (red dots), obtained during the retrieval analysis. The continuous red line shows the best-fitting retrieved model along with $1\sigma$, $2\sigma$ and $3\sigma$ confidence levels. A zoom around the WFC3 is shown in the top left corner.

star, we assumed the same Phoenix stellar model as described in Section 3.2.

For all free parameters in our model we adopted uniform priors with the following ranges: $10^{-5}$ to $10^{-0.5}$ for $\kappa_{\rm IR}$; $10^{-4}$ to $10^{1.5}$ for $\gamma_1$ and $\gamma_2$; 0 to 1 for $\alpha$; and 0 to 2 for $\beta$. For the mixing ratios of chemical species other than H and He, we adopted uniform priors between $10^{-12}$ and 0.05. Our assumption on the metal abundances is motivated by the fact that HAT-P-32Ab is known to be a gas giant (Hartman et al. 2011). Our retrieval analysis proceeded by first identifying the minimum $\chi^2$ solution using non-linear least-squares optimization and then marginalizing over the posterior distribution using differential-evolution Markov chain Monte Carlo (Eastman, Gaudi & Agol 2012). A total of 10 chains for 30 000 steps each, were ran until the Gelman–Rubin statistic for each free parameter was within 1 per cent of unity, showing that the chains were well mixed and had reached a steady state. We discarded a burn-in phase from all chains corresponding to the step at which all chains had found a $\chi^2$ below the median $\chi^2$ value of the chain (Eastman et al. 2012). Finally, we combined the remaining samples into a single chain, forming our posterior distributions.

We found the retrieved abundances of all molecules to be poorly constrained, except for $CH_4$ and VO, which are constrained between 0.5 and 2 orders of magnitude, respectively. The best-fitting model to the data gave $\chi^2 = 11.16$ for 6 degrees of freedom and BIC = 45.8. While $CH_4$ is preferred by the retrieval model, the lower $3\sigma$ bound on the $CH_4$ vertical mixing ratio is $1.1 \times 10^{-7}$. This value is close to the solar-abundance chemical equilibrium value of $CH_4$ at 2000 K and 1-bar (Sharp & Burrows 2007), so we do not have solid evidence for enhanced $CH_4$. Like in the forward-modelling described in Section 3.2, retrieval models also give an isothermal P–T profile as the most favorable scenario, with some inverted profiles included within the $3\sigma$ confidence region. As in Section 3.2, retrieval models also disfavour non-inverted P–T profiles. We report our retrieval results in Figs 4 and 5 along with the MCMC posterior distributions, shown in Fig. C1.

### 3.4 Constraining the albedo and recirculation

The measured brightness temperature ($T_{\rm p}$) and consistency with a blackbody spectrum across a wide wavelength range allows us to explore the planet's bond albedo $A_B$ and redistribution efficiency $\varepsilon$, $0 < \varepsilon < 1$ using the Cowan & Agol (2011) day-side temperature, $T_{\rm d}$ parametrization:

$$T_{\rm d} = T_0(1 - A_B)^{1/4}\left(\frac{2}{3} - \frac{5}{12}\varepsilon\right)^{1/4}, \quad (6)$$

where $T_0 = T_{\rm eff}/\sqrt{a/R_*}$ is the equilibrium temperature at the planet's substellar point (for a circular orbit) and $T_{\rm eff}$ is the effective temperature of HAT-P-32A. Assuming that the day-side temperature, $T_{\rm d}$ is equal to the planet brightness temperature, $T_{\rm p}$ we solved equation (6) for $A_B$ and propagated the uncertainty of $T_{\rm p}$ (Fig. 6).

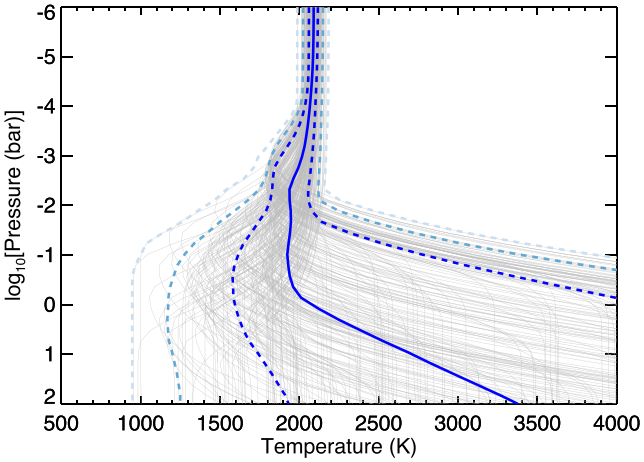


**Figure 5.** P–Tprofiles for HAT-P-32Ab. A subset of P–T profiles sampled during the MCMC retrieval analysis are indicated with the grey continuous lines. The median and $1\sigma$, $2\sigma$ and $3\sigma$ confidence regions are indicated with the blue continuous and dashed lines, respectively.

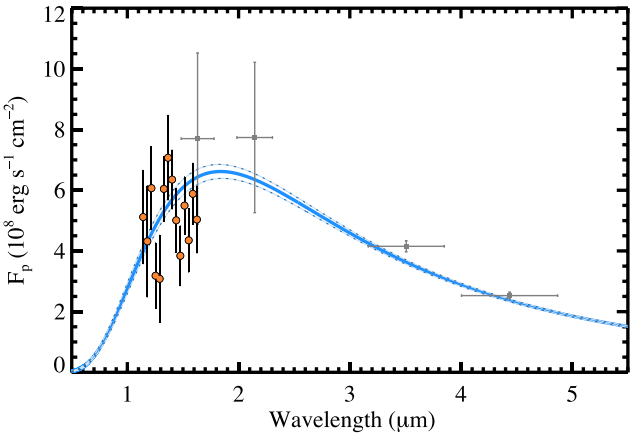


**Figure 7.** Planet thermal emission spectrum of HAT-P-32Ab (orange and grey dots refer to the WFC3 and WIRC+IRAC observations, respectively) along with the best-fitting blackbody curve ($T_p = 1995 \pm 17$ K) and $1\sigma$ uncertainty (blue lines).

Our result rules out a low-albedo low-recirculation scenario for the atmosphere of HAT-P-32Ab. In addition, Fig. 6 also implies that if the the albedo is low the planet would have an efficient recirculation.

Previous findings (Cowan & Agol 2011; Cowan et al. 2012; Perez-Becker & Showman 2013) have shown a tendency towards lower recirculation efficiency and greater day–night temperature contrasts as the stellar irradiation increases. Interestingly for HAT-P-32Ab, a high recirculation of 0.65 is suggested when assuming zero albedo, which given it's high ∼1995 K dayside temperature would go against this trend. In a comprehensive study of 50 short-period transiting giant exoplanets, Schwartz & Cowan (2015) and Schwartz et al. (2017) resolved the albedo versus heat-transport degeneracy for 16 exoplanets from the sample by considering eclipse measurements at optical wavelengths and phase curve data. The authors found evidence for reflective clouds and optical absorbers for some planets like HD189733b while others had very low albedos. Comparing our Fig. 6 to their fig. 7, if HAT-P-32Ab's albedo were low (<0.15) the recirculation would have to be more efficient ($\gtrsim$0.6) than most of the constrained exoplanets, whose recirculation range between about 0.4 and 0.7 in the low albedo regime. Given

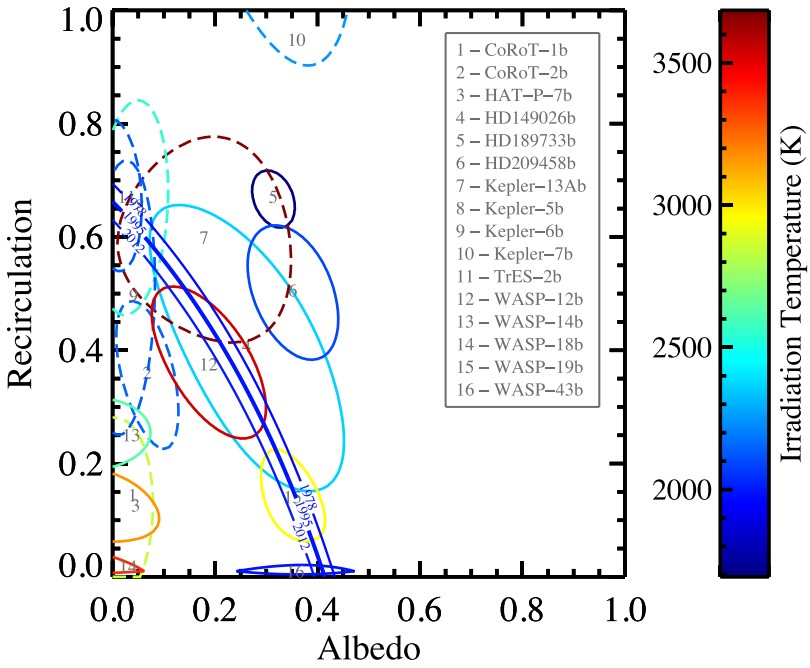


**Figure 6.** Constraints on the planetary albedo and recirculation efficiency of HAT-P-32Ab (blue curve with $1\sigma$ confidence regions) compared to measurements for other 16 gas-giants (closed regions). The main reason for the degeneracy strip instead of a constrained 'island' for HAT-P-32Ab is in the limited constraining power of infrared eclipse observations alone. The degeneracy has been resolved for the 16 exoplanets by combining infrared with optical occultations. Composite $1\sigma$ confidence regions are shown with the horizontal axis measuring different quantities: *Geometric albedo* at visible wavelengths for exoplanets with optical eclipse observations-only (dashed lines) and *Bond albedo* for thermal observation planets (solid lines). The colour bar indicates irradiation temperature, where the red and purple colours correspond to warmer and cooler temperatures, respectively.

the transmission spectrum of the planet indicates the presence of thick clouds (Gibson et al. 2013a; Mallonn et al. 2016; Mallonn & Strassmeier 2016; Nortmann et al. 2016) and the day-side temperature is close to several condensation curves, a high albedo for the planet seems plausible, and could be verified with optical eclipse or phase curve information. Kepler-7b, another low-density bloated exoplanet, has also been shown to have a high albedo in the range 0.4–0.5, over the *Kepler* passband, Garcia Munoz & Isaak (2015). The authors used optical phase curve observations, which enabled constrains on the composition and cloud particle sizes, consistent with condensates of silicates, perovskite and silica of sub-micron radii.

### 3.5 Interpretation

The combined WFC3, WIRC and IRAC day-side thermal emission spectrum of HAT-P-32Ab is compatible with an isothermal blackbody spectrum at a temperature of $T_{\rm p} = 1995 \pm 17$K (BIC = 30.1), but can equally well be described by a model, assuming thermal inversion (BIC = 28.6[2]). The WFC3 observation also shows no evidence of the absorption or emission signature of water at 1.4 μm (Figs 3, 4, 5 and 7). Because the two models can be alternative explanations of our observations, and are both nearly equally likely statistically, we discuss the possible scenarios for the atmosphere of the planet assuming each of them.

#### *3.5.1 Isothermal spectrum*

In the case of an isothermal spectrum, there are two distinct scenarios for the atmosphere of the planet. In the first scenario, the spectrum probes pressure levels with a constant temperature, equal to the measured blackbody temperature. A constant temperature with altitude can be maintained if a cooling and heating mechanisms balance in the probed atmospheric layers. For a clear atmosphere with a decreasing temperature profile, this can be the case of an absorber that traps stellar radiation and effectively modifies the profile to resemble an isothermal or a profile with weak inversion (i.e. increasing temperature with altitude). Prime candidates for the hypothetical absorber could be the spectroscopically active TiO and VO, expected to be in a gas phase at the day-side temperature of the planet (Fortney et al. 2008; Lodders 1999). Such balancing conditions are known to occur in the transition atmospheric layers, e.g. tropopause, stratopause, mesopause, etc. of Solar system planets with rather limited depth of the order of a few tens kilometres. If our combined emission spectrum is produced by such a hypothetical transition layer its depth would be substantial, ranging from ∼3 bar to ∼3 mbar.

In the second scenario, the observed isothermal spectrum could probe one and the same pressure level. In this case, the spectrum could be produced by a thick dusty cloud deck covering the day-side, with a temperature on its top equal to the measured blackbody temperature. Near-infrared secondary eclipse observations can probe layers deep in the day-side of the atmosphere reaching a few bars. However, in the case of a high-altitude cloud deck distinguishing between a high-altitude versus low-altitude cloud deck could virtually be impossible should the grain sizes are comparable or larger than the wavelength (e.g. microns). In the case of a low-altitude cloud deck, the layers above it could contribute with absorption or emission lines, should the layer temperature be lower or higher than the temperature of the deck, respectively. Our comparative analysis with models showed that absorption lines would easily be detectable, but are not present. There is still the possibility of hotter layers, contributing with emission lines, above the cloud deck, but their detection would be challenging at the precision of the data. Hence, we cannot distinguish between low-altitude and high-altitude cloud deck.

A cloudy day-side scenario would also agree with the evidence for clouds at the averaged day–night terminator. Featureless flat optical transmission spectroscopy from 0.3 to 1 μm has been reported by a number of studies, e.g. Gibson et al. (2013a), Mallonn et al. (2016), Mallonn & Strassmeier (2016) and Nortmann et al. (2016) along with a recent detection of nearly half reduced amplitude water feature at 1.4 μm from *HST* WFC3 transmission spectroscopy (Tsiaras et al. 2017). Those observations imply a high-altitude dust deck or a layer of haze with grain sizes comparable to the wavelength of the the visible light. Due to the larger wavelength in the near-infrared the radiation starts to penetrate to deeper layers, which can explain the reduced water feature. Given the equilibrium temperature of the planet 1786 ± 26 K, potential condensate forming species at the cooler day-side terminator include the silicate condensates enstatite and forsterite (Lodders 1999). However, it should be noted that clouds at the terminator do not necessarily imply clouds on the day-side due to the significant differences in the temperature and altitude.

A third possible scenario to produce the observed blackbody spectrum would require a combination of partially clear and cloudy day-side atmosphere. This scenario is plausible given the fact that secondary eclipse observations probe also the region of the atmosphere around the planet's hotspot, which has been predicted to be free of clouds, due to its high temperature and strong winds (Parmentier et al. 2016).

#### *3.5.2 An atmosphere with thermal inversion*

A model atmosphere with thermal inversion is an alternative explanation for the observed emission spectrum. An optical absorber could produce significant heating in the upper atmosphere to either cause an inversion or be near-isothermal over a large pressure range. VO is favoured by the data at vertical mixing ratio (VMR) of $2.3 \times 10^{-7}$ (30 × solar) and matches the WFC3 features, though the lower abundance range is unconstrained. Presence of VO would be consistent with inverted scenario in which the day-side atmosphere is cloud-free. The signature of VO instead of water can be explained by the fact that the cross-section of VO is several orders of magnitude larger than the cross-section of water at the WFC3 wavelengths (Evans et al. 2017).

#### *3.5.3 Future observations*

Since planetary occultations only offer information of the day side, they cannot resolve the circulation-Bond albedo degeneracy. Optical secondary eclipse or phase curve observations or alternatively infrared phase curves can help resolve this degeneracy. In addition, observations at higher signal to noise ratio and complementary wavelength regions can further shed light on the atmosphere of the planet. In particular, observations with the *James-Webb Space Telescope* (*JWST*) can help resolve the three case scenario by detecting the signature of clouds at mid-infrared wavelengths. WFC3 hints at low-amplitude molecular features in the spectrum which could be resolved. The thermal emission spectrum of HAT-P-32Ab

[2] Bayesian Information Criterion, Schwarz (1978).

joins a significant sample of isothermal spectra reported in the literature (e.g. Crouzet et al. 2014; Stevenson et al. 2014b; Cartier et al. 2017).

## 4 CONCLUSIONS

We reported *HST* WFC3 emission spectrum of HAT-P-32Ab covering the wavelength range from 1.123 to 1.644 μm. Combined with previous thermal eclipse observations, our spectrum can equally well be described by an isothermal blackbody spectrum with a temperature of $T_p = 1995 \pm 17$ K or a model assuming thermal inversion layer. A comparative and retrieval analysis with 1D radiative-convective atmospheric models excludes models, assuming non-inverted temperature profiles at a high confidence. A blackbody or thermally inverted emission spectrum can imply several alternative scenarios for the planetary atmosphere, including (i) clear atmosphere with absorber, (ii) dusty cloud deck or (iii) combination of both. Eclipse observations with the JWST could help to potentially resolve the three-case degeneracy for the day-side atmosphere of the planet. Converting the measured blackbody temperature to brightness temperature, we find that the planet can have continuum of values for the albedo and recirculation, ranging from high albedo and poor recirculation (bright and still) to low albedo but very efficient recirculation (dark and windy). Optical eclipse observations could help to resolve the albedo versus recirculation degeneracy and shed more light on the presence or absence of clouds on the day-side of the planet.

## ACKNOWLEDGEMENTS

The authors are happy to thank D. Foreman-Mackey, J. Schwartz and V. Parmentier for fruitful discussions and help during the course of this work. This work is based on observations with the NASA/ESA *Hubble Space Telescope*, obtained at the Space Telescope Science Institute (STScI) operated by AURA, Inc. This work is based in part on observations made with the *Spitzer Space Telescope*, which is operated by the Jet Propulsion Laboratory, California Institute of Technology under a contract with NASA. NN, DKS and TME acknowledge funding from the European Research Council under the European Unions Seventh Framework Programme (FP7/2007-2013)/ERC grant agreement no. 336792. JG acknowledges support from a Leverhulme Trust Research Project Grant. G.W.H. and M.H.W. acknowledge long-term support from Tennessee State University and the State of Tennessee through its Centers of Excellence program and from the Space Telescope Science Institue under HST-GO-14767. This work has been carried out in the frame of the National Centre for Competence in Research PlanetS supported by the Swiss National Science Foundation (SNSF). DE and VB acknowledge the financial support of the SNSF. This project has received funding from the European Research Council (ERC) under the European Union's Horizon 2020 research and innovation programme (project FOUR ACES; grant agreement No 724427).

## REFERENCES

Adams E. R., Dupree A. K., Kulesa C., McCarthy D., 2013, AJ, 146, 9
Albrecht S. et al., 2012, ApJ, 757, 18
Allard F., Homeier D., Freytag B., 2012, Phil. Trans. R. Soc. A, 370, 2765
Ambikasaran S., Foreman-Mackey D., Greengard L., Hogg D. W., O'Neil M., 2014, IEEE Trans. Pattern Anal. Mach. Intell., 38, 2
Amundsen D. S., Baraffe I., Tremblin P., Manners J., Hayek W., Mayne N. J., Acreman D. M., 2014, A&A, 564, A59
Amundsen D. S., Tremblin P., Manners J., Baraffe I., Mayne N. J., 2017, A&A, 598, A97
Burrows A., Hubeny I., Budaj J., Knutson H. A., Charbonneau D., 2007, ApJ, 668, L171
Cartier K. M. S. et al., 2017, AJ, 153, 34
Cowan N. B., Agol E., 2011, ApJ, 729, 54
Cowan N. B., Machalek P., Croll B., Shekhtman L. M., Burrows A., Deming D., Greene T., Hora J. L., 2012, ApJ, 747, 82
Crouzet N., McCullough P. R., Deming D., Madhusudhan N., 2014, ApJ, 795, 166
Deming D. et al., 2013, ApJ, 774, 95
Drummond B., Tremblin P., Baraffe I., Amundsen D. S., Mayne N. J., Venot O., Goyal J., 2016, A&A, 594, A69
Eastman J., Gaudi B. S., Agol E., 2012, Astrophysics Source Code Library, record ascl:1207.001
Eaton J. A., Henry G. W., Fekel F. C., 2003, in Oswalt T. D., ed., Astrophysics and Space Science Library, Vol. 288, Astrophysics and Space Science Library. Kluwer Academic Publishers, Dordrecht, p. 189
Evans T. M. et al., 2016, ApJ, 822, L4
Evans T. M. et al., 2017, Nature, 548, 58
Foreman-Mackey D., 2015, Astrophysics Source Code Library, record ascl:1511.015
Foreman-Mackey D., 2016, J. Open Source Softw., 24
Foreman-Mackey D., Hogg D. W., Lang D., Goodman J., 2013, PASP, 125, 306
Fortney J. J., Marley M. S., 2007, ApJ, 666, L45
Fortney J. J., Lodders K., Marley M. S., Freedman R. S., 2008, ApJ, 678, 1419
Fortney J. J., Shabram M., Showman A. P., Lian Y., Freedman R. S., Marley M. S., Lewis N. K., 2010, ApJ, 709, 1396
Garcia Munoz A., Isaak K. G., 2015, Proc. Natl. Acad. Sci., 112, 13461
Gibson N. P., Aigrain S., Barstow J. K., Evans T. M., Fletcher L. N., Irwin P. G. J., 2013a, MNRAS, 428, 3680
Gibson N. P., Aigrain S., Barstow J. K., Evans T. M., Fletcher L. N., Irwin P. G. J., 2013b, MNRAS, 436, 2974
Gibson N. P., Nikolov N., Sing D. K., Barstow J. K., Evans T. M., Kataria T., Wilson P. A., 2017, MNRAS, 467, 4591
Goyal J. et al., 2017, MNRAS, 999, X99
Guillot T., 2010, A&A, 520, A27
Hartman J. D. et al., 2011, ApJ, 742, 59
Haynes K., Mandell A. M., Madhusudhan N., Deming D., Knutson H., 2015, ApJ, 806, 146
Heng K., 2017, Exoplanetary Atmospheres: Theoretical Concepts and Foundations. Princeton Univ. Press, Princeton
Henry G. W., 1999, PASP, 111, 845
Hubeny I., Burrows A., Sudarsky D., 2003, ApJ, 594, 1011
Huitson C. M. et al., 2013, MNRAS, 434, 3252
Knutson H. A., Charbonneau D., Allen L. E., Burrows A., Megeath S. T., 2008, ApJ, 673, 526
Knutson H. A. et al., 2014, ApJ, 785, 126
Kreidberg L. et al., 2015, ApJ, 814, 66
Kurucz R. L., 1979, ApJS, 40, 1
Line M. R. et al., 2013, ApJ, 775, 137
Line M. R., Knutson H., Wolf A. S., Yung Y. L., 2014, ApJ, 783, 70
Line M. R. et al., 2016, AJ, 152, 203
Lodders K., 1999, ApJ, 519, 793
Madhusudhan N., Seager S., 2009, ApJ, 707, 24
Madhusudhan N., Knutson H., Fortney J. J., Barman T., 2014, Protostars and Planets VI. Univ. Arizona Press, Tucson, p. 739
Mallonn M., Strassmeier K. G., 2016, A&A, 590, A100
Mallonn M. et al., 2016, MNRAS, 463, 604
Mandel K., Agol E., 2002, ApJ, 580, L171
Nikolov N. et al., 2014, MNRAS, 437, 46
Nikolov N. et al., 2015, MNRAS, 447, 463
Nikolov N., Sing D. K., Gibson N. P., Fortney J. J., Evans T. M., Barstow J. K., Kataria T., Wilson P. A., 2016, ApJ, 832, 191
Nortmann L., Pallé E., Murgas F., Dreizler S., Iro N., Cabrera-Lavers A., 2016, A&A, 594, A65
Parmentier V., Fortney J. J., Showman A. P., Morley C., Marley M. S., 2016, ApJ, 828, 22
Perez-Becker D., Showman A. P., 2013, ApJ, 776, 134

Pont F., Sing D. K., Gibson N. P., Aigrain S., Henry G., Husnoo N., 2013, MNRAS, 432, 2917
Schwartz J. C., Cowan N. B., 2015, MNRAS, 449, 4192
Schwartz J. C., Kashner Z., Jovmir D., Cowan N. B., 2017, ApJ, preprint (arXiv:1707.05790)
Schwarz G., 1978, Ann. Stat., 6, 461
Seager S., 2010, Exoplanet Atmospheres: Physical Processes
Sharp C. M., Burrows A., 2007, ApJS, 168, 140
Sing D. K. et al., 2011, MNRAS, 416, 1443
Sing D. K. et al., 2012, MNRAS, 426, 1663
Sing D. K. et al., 2015, MNRAS, 446, 2428
Sing D. K. et al., 2016, Nature, 529, 59
Stevenson K. B. et al., 2014a, Science, 346, 838
Stevenson K. B., Bean J. L., Madhusudhan N., Harrington J., 2014b, ApJ, 791, 36
Tremblin P., Amundsen D. S., Mourier P., Baraffe I., Chabrier G., Drummond B., Homeier D., Venot O., 2015, ApJ, 804, L17
Tremblin P., Amundsen D. S., Chabrier G., Baraffe I., Drummond B., Hinkley S., Mourier P., Venot O., 2016, ApJ, 817, L19
Tsiaras A. et al., 2017, ApJ, preprint (arXiv:1704.05413)
Wakeford H. R. et al., 2017, ApJ, 835, L12
Winn J. N., 2010, preprint (arXiv:1001.2010)
Zellem R. T. et al., 2017, ApJ, 844, 27
Zhao M. et al., 2014, ApJ, 796, 115
Zhou Y., Apai D., Lew B. W. P., Schneider G., 2017, AJ, 153, 243

## APPENDIX A: WHITE LIGHT-CURVE MCMC POSTERIOR DISTRIBUTIONS

In this appendix, we present posterior distributions of the variable eclipse parameters and hyperparameters from the MCMC chains for the white light curve of HAT-P-32Ab (Fig. A1).

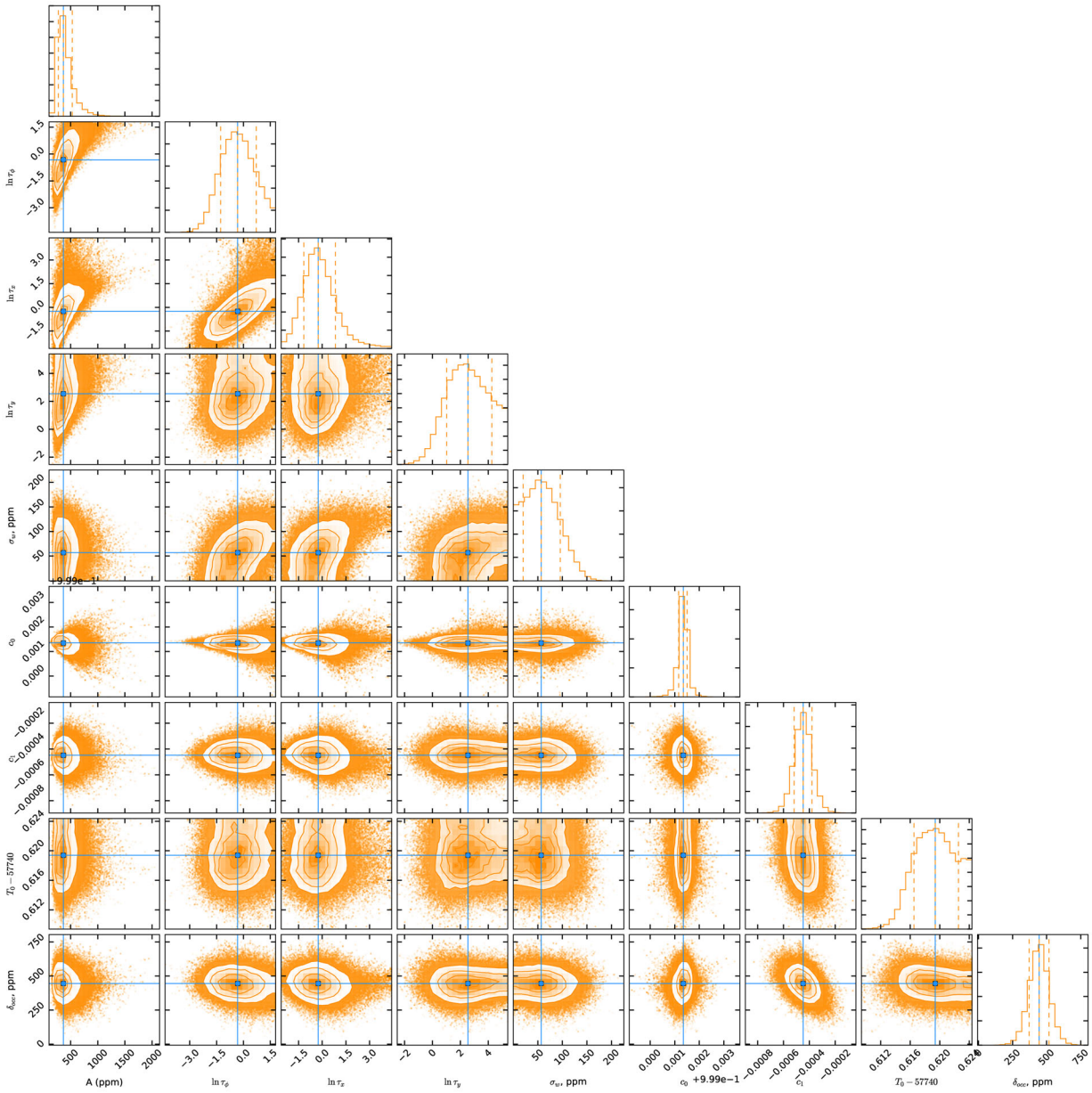


**Figure A1.** Posterior distributions of the variable eclipse parameters and hyperparameters from the MCMC chains for the white light curve. The scatter plots show all pairs of parameters plotted after marginalization over all other parameters, and the histograms show the marginalized posterior distribution of each individual parameter. The median and $1\sigma$ measured parameters are indicated with continuous and dashed lines, respectively.

## APPENDIX B: SPECTROSCOPIC LIGHT CURVES

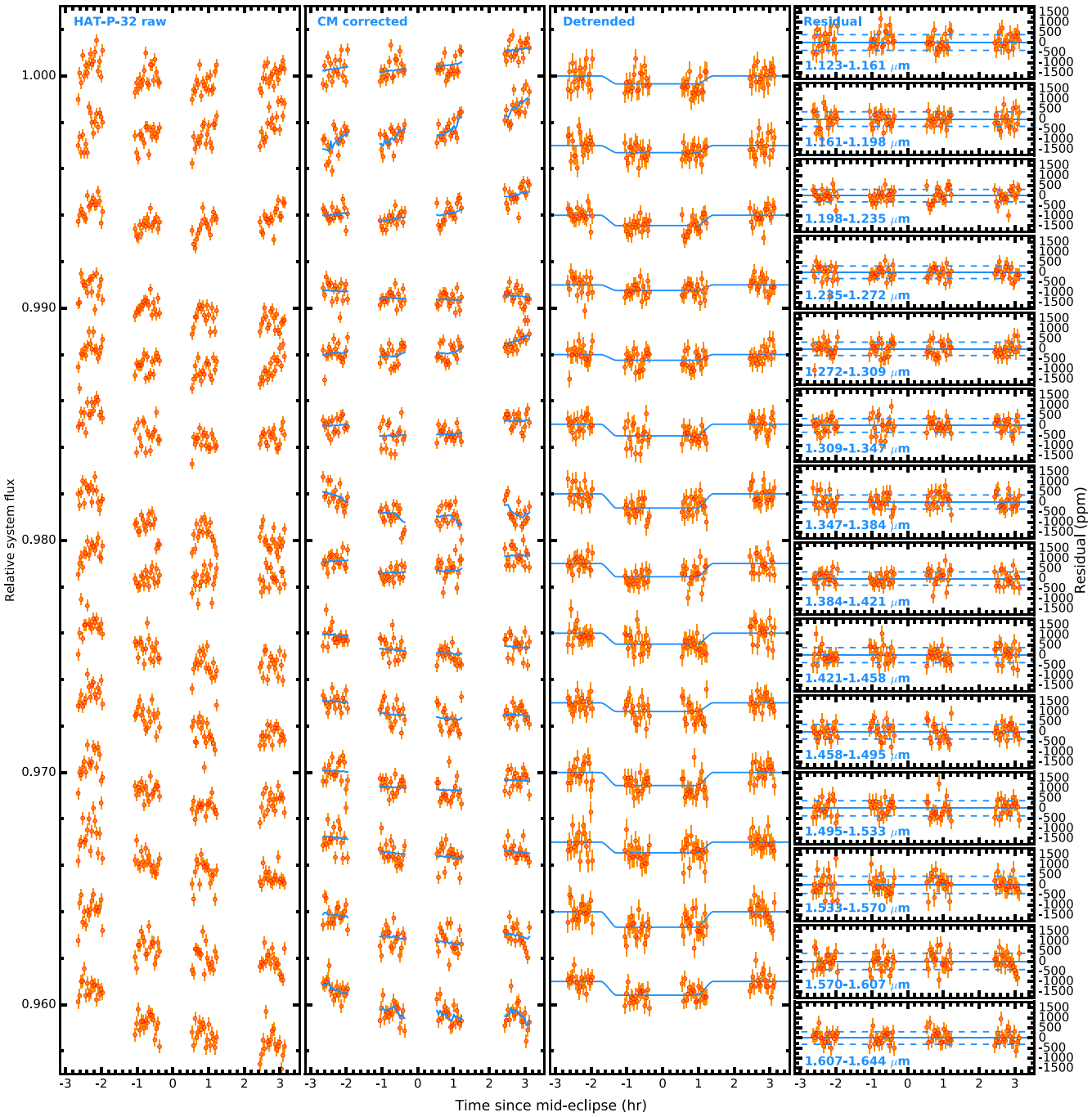


**Figure B1.** Spectroscopic light curves for HAT-P-32Ab. First panel: raw normalized light curves. Second panel: common-mode corrected raw light curves along with the best-fitingt GP systematics and eclipse model. Third panel: detrended eclipse light curves along with an eclipse model calculated from the marginalized posterior distributions. Small panels: light-curve residuals with error bars from each fit.

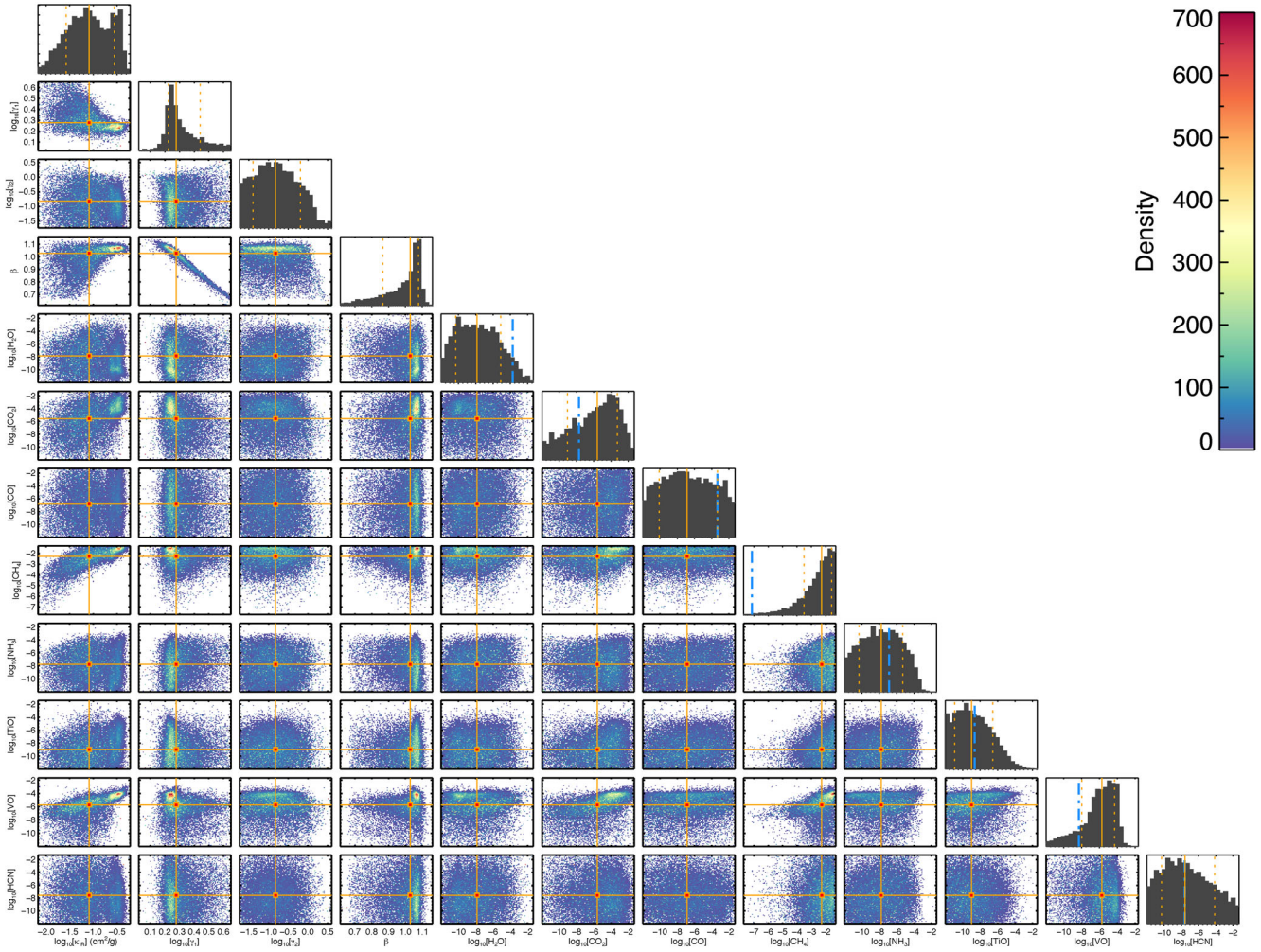


**Figure C1.** Posterior distributions from the MCMC retrieval analysis. The scatter plots show all pairs of parameters plotted after marginalization over all other parameters, and the histograms show the marginalized posterior distribution of each individual parameter. The median and 1$\sigma$ measured parameters are indicated with continuous and dashed lines, respectively. The dash–dotted lines represent the solar abundances, calculated with ATMO, assuming solar metallicity and solar C/O ratio and a recirculation factor of 0.75 at 1 bar with rainout.

## APPENDIX C: RETRIEVAL RESULTS

[1]*Physics and Astronomy, University of Exeter, EX4 4QL Exeter, UK*
[2]*Tennessee State University, 3500 John A. Merritt Blvd., PO Box 9501, Nashville, TN 37209, USA*
[3]*Harvard-Smithsonian Center for Astrophysics, 60 Garden Street, Cambridge, MA 02138, USA*
[4]*Zentrum für Astronomie und Astrophysik, Technische Universität Berlin, D-10623 Berlin, Germany*
[5]*Sorbonne Universités, UPMC Université Paris 6 and CNRS, UMR 7095, Institut d'Astrophysique de Paris, 98 bis boulevard Arago, F-75014 Paris, France*
[6]*Centro de Astrobiología (CSIC-INTA), ESAC Campus, Camino bajo del Castillo, E-28692 Villanueva de la Cañada, Madrid, Spain*
[7]*Lunar and Planetary Laboratory, University of Arizona, Tucson, AZ 85721, USA*
[8]*NASA Jet Propulsion Laboratory, 4800 Oak Grove Drive, Pasadena, CA 91109, USA*
[9]*Department of Physics and Astronomy, University College London, Gower Street, London WC1E 6BT, UK*
[10]*Observatoire de l'Université de Genève, 51 chemin des Maillettes, CH-1290 Sauverny, Switzerland*
[11]*Centre for Star and Planet Formation, Niels Bohr Institute and Natural History Museum, University of Copenhagen, DK-1350 Copenhagen, Denmark*
[12]*Lowell Center for Space Science and Technology, University of Massachusetts, Lowell, MA 01854, USA*
[13]*Department of Astronomy, University of Maryland, College Park, MD 20742 USA*
[14]*Division of Geological and Planetary Sciences, California Institute of Technology, Pasadena, CA 91125 USA*
[15]*Groupe de Spectroscopie Moléculaire et Atmosphérique, Université de Reims, Champagne-Ardenne, CNRS UMR F-7331, France*
[16]*Space Telescope Science Institute, 3700 San Martin Drive, Baltimore, MD 21218, USA*
[17]*NASA Goddard Space Flight Center, Greenbelt, MD 20771, USA*

This paper has been typeset from a TEX/LATEX file prepared by the author.